Metals and Materials International (2020) 26:1872–1880
https://doi.org/10.1007/s12540-019-00474-1

Structural Understanding of $MnO–SiO_2–Al_2O_3–Ce_2O_3$ Slag via Raman, ^{27}Al NMR and X-ray Photoelectron Spectroscopies

Tae Sung Kim[1] · Se Ji Jeong[1,2] · Joo Hyun Park[1]

Received: 7 July 2019 / Accepted: 20 September 2019 / Published online: 4 October 2019

Abstract
In order to understand sulfur solubility in the $MnO–SiO_2–Al_2O_3–Ce_2O_3$ slag or inclusion system (mol MnO/mol SiO_2 = M/S = 2.2 or 0.9, Al_2O_3 = 14.2[± 1.8] mol%, Ce_2O_3 = 0–5.6 mol%), the effect of Ce^{3+} ions on the structure of the Mn–aluminosilicate system with different M/S molar ratios has been studied by micro-Raman spectroscopy, solid-state nuclear magnetic resonance (NMR) spectroscopy and X-ray photoelectron spectroscopy (XPS). Because constant oxygen partial pressure was maintained at $p(O_2) = 2.8 \times 10^{-7}$ atm, oxidation state of Mn and Ce would be in Mn^{2+} and Ce^{3+} in the $MnO–SiO_2–Al_2O_3–Ce_2O_3$ system, which were also confirmed by XPS analysis. Although it was difficult to measure the ^{27}Al solid-state NMR spectra of the quenched $MnO–SiO_2–Al_2O_3$ system due to the paramagnetic effect, ^{27}Al NMR spectra did show structural changes in aluminate when cerium was added to the Mn–aluminosilicate melts. Addition of Ce_2O_3 in the high M/S(= 2.2) system caused both an explosive enhancement in the intensity of Raman bands at 600 cm^{-1} and a peak shift in ^{27}Al NMR spectra, indicating the transition from the $[AlO_4]^-$:$0.5Mn^{2+}$ tetrahedron to a $[AlO_6]^{3-}$:Ce^{3+} octahedron complex due to a strong attraction between aluminate and the cerium ion. XPS spectra show that the transition of the aluminate structure upon introduction of Ce^{3+} ions consumes free oxygen in Mn–aluminosilicate melts in high M/S(= 2.2) system. However, the same structural changes were not observed when Ce_2O_3 was added to lower M/S(= 0.9) system, because Ce^{3+} ions primarily interact with the pre-existing $[AlO_6]$-octahedron in low M/S system.

Keywords Raman spectroscopy · ^{27}Al NMR spectroscopy · X-ray photoelectron spectroscopy · $MnO–SiO_2–Al_2O_3–Ce_2O_3$ slag or inclusion · Octahedron · Tetrahedron

1 Introduction

It is very important to control sulfur contents in molten steel because the uptake of sulfide or oxy-sulfide type inclusions deteriorates the corrosion resistance and mechanical behavior of steels [1, 2]. Sulfur could be effectively removed from molten steel by a liquid oxide slag and/or inclusion system containing rare earth elements, which has a high solubility for sulfur because of strong attraction between rare earth elements and sulfur at temperatures that are typical for steelmaking.

Anacleto et al. [3] investigated the effect of Ce oxide on the sulfide capacity of the $CaO–SiO_2$ slag from the slag-metal reaction between $CaO–SiO_2–Ce_2O_3$ slag and carbon saturated iron at 1773 K. It was concluded that the addition of Ce oxide to $CaO–SiO_2$ slag is more effective on desulfurization than that of CaO because it decreases the activity coefficient of SiO_2 in the slags. Yang et al. [4] presented that substituting Ce_2O_3 for Al_2O_3 in the $CaO–Al_2O_3–SiO_2–MgO$ (CaO/Al_2O_3 = 1.5, SiO_2 = 10 wt%, MgO = 7 wt%) slag has positive effect on desulfurization in Al-killed steel at 1873 K because increase in Ce_2O_3 content improves the fluidity of molten slags. Nevertheless, it is not clear to understand the effect of Ce_2O_3 on sulfide capacity of the slags in a thermodynamics standpoint in these previous studies.

In our previous study [5], the sulfide capacity of the $MnO–SiO_2–Al_2O_3–Ce_2O_3$ (MnO/SiO_2 = 0.3–2.2 molar ratio) quaternary system was measured by the gas-slag equilibration method at 1873 K in order to evaluate the effect of Ce oxide on the sulfur speciation behavior in

✉ Joo Hyun Park
basicity@hanyang.ac.kr

[1] Department of Materials Engineering, Hanyang University, Ansan 15588, Republic of Korea

[2] Process Research Group, R&D Center, SeAH CSS Corp., Changwon 51708, Republic of Korea

the quaternary system. The addition of Ce_2O_3 to the $MnO–SiO_2–Al_2O_3–Ce_2O_3$ quaternary system at high basicity compositions (i.e., $MnO/SiO_2 > 1$, molar ratio) decreased the sulfide capacity of the quaternary system unlike the results of Anacleto et al. and Yang et al. Because there is limited thermodynamic information for the cerium oxide containing slags such as activity of components, phase diagrams, etc., the short range order structural units of the system was analyzed using micro-Raman spectroscopy, which was widely employed to investigate MnO-containing silicate melts [6–9], in order to understand the role of Ce_2O_3 for the solubility of sulfur [5]. Nevertheless, the structure of the $MnO–SiO_2–Al_2O_3–Ce_2O_3$ system poses more open questions that warrant further investigation.

Many researchers sought to investigate oxide melts, glasses and crystals containing transition metal or rare earth cations using solid-state nuclear magnetic resonance (NMR) spectroscopy [10–25]. The presence of paramagnetic cations significantly broadens NMR peaks, accompanied by a loss of peak intensity [14, 15, 21]. Kim et al. [15, 21] propose that the spectra of iron-bearing glass do not provide clear resolution of multiple Si environments because the intensity of peaks from iron-bearing glass decrease and broaden with increasing Fe_2O_3 content. Signal loss and peak broadening are primarily due to a strong effect of the unpaired electrons in the *d*-orbitals of Fe on the decrease of spin–lattice relaxation time of Si nuclear [15, 21].

The strong interaction between the unpaired electrons in the paramagnetic cation and the observed nuclear spins could either positively and negatively shift the NMR peaks [10–25]. It has been discussed that the paramagnetic shifts are caused by Fermi contact shift (through-bond transfer of unpaired electron spin density) and/or pseudo contact shift (through-space dipolar coupling from a magnetic cation in an asymmetrical site) [10–12, 16–18, 22–24]. It is observed that the number of unpaired electrons for M cation ($M = Mn^{2+}$, Fe^{2+}, Co^{2+}, Ni^{2+}) strongly affects the increase in paramagnetic shifts in ^{31}P or ^{29}Si NMR peaks for Li-phosphate olivine ($LiMPO_4$) or silicate olivine (M_2SiO_4) [13, 19, 25]. For investigating the structure of Ce doped yttrium aluminum garnet (YAG) using ^{27}Al NMR spectroscopy, Ce^{3+} cations, which are neighbored near [AlO_4] and [AlO_6]-units, also cause the paramagnetic shifts in the ^{27}Al NMR peaks [18, 22, 24]. Therefore, it is expected that the manganese and cerium cations in the $MnO–SiO_2–Al_2O_3–Ce_2O_3$ system would result in the paramagnetic shifts in ^{27}Al NMR peaks.

Because the radius of Ce^{3+} ion ($r = 1.01$ Å) is too large to be a network former such as [SiO_4]- tetrahedrally coordinated units and is similar to that of Ca^{2+} ($r = 1.0$ Å) or Na^+ ($r = 1.02$ Å), Lin et al. [26, 27] proposed that the Ce^{3+} ion has a preference to be charge compensator or network modifier. Wu and Pelton [28] reported strong interaction between Ce_2O_3 and Al_2O_3 from the evaluation of phase diagram for $R_2O_3–Al_2O_3$ (R: Rare earth) binary systems. It was also revealed that the activity coefficient of Al_2O_3 declines with the increase in Ce_2O_3 content in the $CaO–Al_2O_3$ melts at 1773 K due to a strong attraction between Ce_2O_3 and Al_2O_3 [29, 30]. Hence, it is conclusive that the Ce_2O_3 has a strong interaction to Al_2O_3 in the present Mn–aluminosilicate system.

In the present study, structural analysis of the $MnO–SiO_2–Al_2O_3–Ce_2O_3$ quaternary system with different MnO/SiO_2 (M/S = 0.9 and 2.2) ratio has been systematically carried out using micro-Raman spectroscopy, ^{27}Al magic angle spinning-nuclear magnetic resonance (MAS-NMR) spectroscopy and X-ray photoelectron spectroscopy (XPS) to elucidate the effect of cerium oxide on the structural changes in Mn–aluminosilicate system quenched from 1873 K.

2 Experimental Procedures

2.1 Preparation of Oxide Samples

A super-kanthal vertical electric furnace was applied to prepare the $MnO–SiO_2–Al_2O_3–Ce_2O_3$ melt at 1873 K. A proportional integral differential controller connected with B-type thermocouple was used in the vertical furnace to control the temperature. Before all of the experiments was carried out, the temperature inside the furnace was checked using an external B-type thermocouple. The mixtures of reagent-grade MnO, SiO_2, Al_2O_3, and CeO_2 were used to manufacture the glass samples. The oxide mixture (1.2 g) in a platinum crucible held in a porous alumina holder was positioned at the hot zone of the furnace under $CO–CO_2$–Ar gas mixture (total flow rate = 400 mL/min) for 12 h. Constant oxygen partial pressure was maintained at $p(O_2) = 2.8 \times 10^{-7}$ atm using a $CO–CO_2$ reaction, i.e., $CO(g) + 1/2O_2(g) = CO_2(g)$, during the equilibration of the oxide melt with the gas mixture at 1873 K.

After 12 h, the platinum crucible containing the oxide mixture was quenched by dipping it into brine. The quenched samples were ground under 100 μm using a crusher for spectroscopic analysis. The compositions of the quenched samples were confirmed using a Bruker S4 explorer X-ray fluorescence spectrometer and the results are listed in Table 1. X-ray diffraction (XRD, D/Max-2500/PC, Rigaku) analysis was carried out to confirm whether the samples were glassy (amorphous) or not. Monochromatized Cu k-alpha radiation was used as the X-ray sauce ($\lambda = 1.5418$ Å) and operated at 40 kV and 100 mA. One representative XRD result is shown in Fig. 1, from reflecting the amorphous nature of all the samples were homogeneous liquids at 1873 K.

Table 1 Experimental composition of oxide samples (mol%)

MnO/SiO_2	MnO	SiO_2	Al_2O_3	Ce_2O_3
2.2	57.4	26.6	16.0	0.0
	57.8	26.2	14.8	1.2
	58.7	23.6	15.1	2.7
	54.4	26.5	15.4	3.7
	55.1	24.8	14.5	5.6
0.9	40.6	44.9	14.5	0.0
	45.0	40.9	13.0	1.1
	46.5	39.5	11.6	2.4
	36.3	46.1	14.0	3.6
	37.5	44.3	13.1	5.0

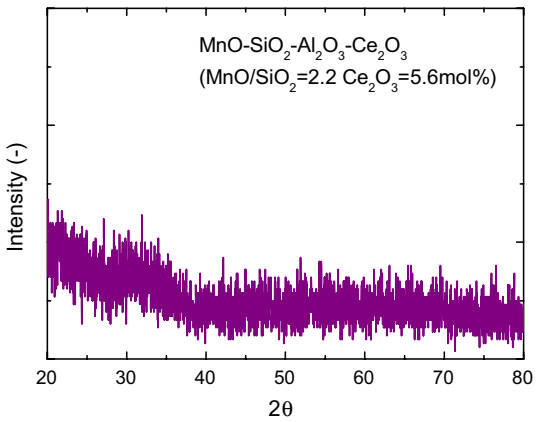

Fig. 1 Typical XRD pattern of the quenched $MnO–SiO_2–Al_2O_3–Ce_2O_3$ ($MnO/SiO_2 = 2.2$) glass sample

2.2 Structural Analysis of Quenched Samples Using Spectroscopic Methodologies

Micro-Raman spectroscopic analysis was carried out using a 'LabRam Aramis' Horiba Jobin–Yvon spectrometer. The 514-nm Ar-ion laser source was used for Raman scattering measurements of the quenched oxide samples. Further details on the preparation, measurement procedure and data processing are available in our previous articles [6–9]. The ^{27}Al NMR spectra were collected using a Bruker Avance II 500 MHz solid-state NMR spectrometer at 11.7 T with a 4-mm-thick wall zirconia rotor and a Doty Scientific double-resonance MAS probe at a spin rate of 10 kHz. The ^{27}Al NMR spectra were collected at radio-frequency fields of 130.32 MHz and with single pulse acquisition with a pulse length of 2.0 µs (radio frequency tip angle of 30°). The recycle delay was 1 s for all samples.

The Mn2p, Ce3d and O1s XPS spectra of the quenched oxide samples were measured using an XPS analyzer (K-alpha by Thermo UK). Monochromatized Al K-α radiation (1486.6 eV) was used as the X-ray source and operated at 3 mA and 12 kV. The rod-shaped samples were fractured in ultrahigh vacuum (4.8×10^{-7} Pa). The surface charge was neutralized by flooding electrons. In order to correct for the charging effects, measured binding energies were calibrated using the binding energy of the adventitious C1s line assuming that the C1s core level is 284.6 eV.

It was confirmed that the oxidation state of Mn would be Mn^{2+} in the present $MnO–SiO_2–Al_2O_3$ system from the observation of Mn^{2+} peaks (642 eV and 654 eV) and MnO satellite feature in Mn2p XPS spectra in Fig. 2a. It was also confirmed that the cerium ion is stabilized as Ce^{3+} in the present system under the reducing atmosphere at 1873 K because the intensity of Ce^{3+} peaks (886.4 and 904.3 eV) is majorly detected in conjunction with relatively small intensity of Ce^{4+} peaks (916 eV) in Fig. 2b.

A typical deconvolution result of the O1s binding energy (eV) from XPS spectra for the $MnO–SiO_2–15.4Al_2O_3–3.7Ce_2O_3$ (mol%, $MnO/SiO_2 = M/S = 2.2$) system is shown in Fig. 3. On the basis of the Gaussian function, the O1s XPS spectra have been deconvoluted into three peaks at about

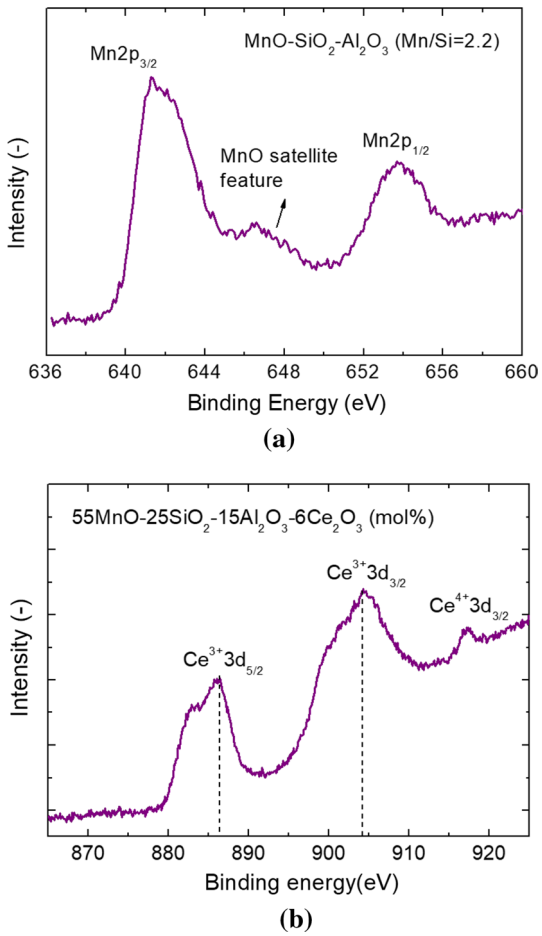

Fig. 2 The XPS spectra of **a** Mn 2p and **b** Ce 3d core level for quenched oxide sample

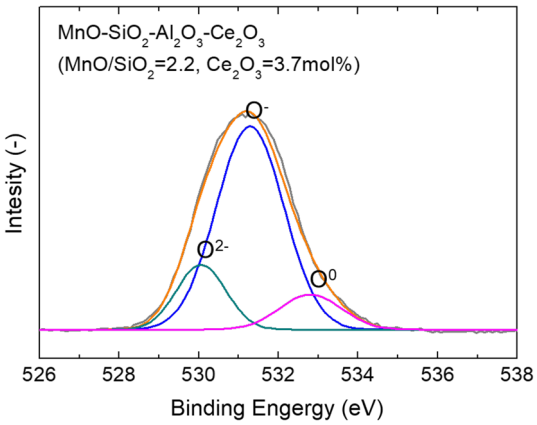

Fig. 3 A typical Gaussian deconvolution result of the O1s binding energy (eV) for the quenched $MnO–SiO_2–Al_2O_3–Ce_2O_3$ ($MnO/SiO_2 = 2.2$) system

530 eV, 531 eV and 532 eV, which correspond to free oxygen (O^{2-}), non-bridging oxygen (O^-) and bridging oxygen (O^0), respectively [31–33]. The free oxygen is defined as binding energy of MnO in the O1s XPS spectra because O^{2-} ions has ionic bonding with MnO in the $MnO–SiO_2–Al_2O_3–Ce_2O_3$ system. The commercial software 'PeakFit' was used for deconvolution of the spectra with an r^2 value over 0.99.

3 Results and Discussion

3.1 Effect of MnO on ^{27}Al NMR Spectroscopy in $MnO–SiO_2–Al_2O_3$ System

In order to understand the effect of the paramagnetic cation, i.e. Mn^{2+}, on ^{27}Al NMR peaks, ^{27}Al NMR spectra of the $MnO–SiO_2–Al_2O_3$ system ($MnO/SiO_2 = 0.9$ molar ratio, $Al_2O_3 = 14$ mol%) are shown in Fig. 4 in conjunction with ^{27}Al NMR spectra of the $CaO–SiO_2–Al_2O_3$ system ($CaO/SiO_2 = 1$ molar ratio, $Al_2O_3 = 13$ mol%). It is difficult to distinguish the ^{27}Al NMR spectra in the $MnO–SiO_2–Al_2O_3$ system in Fig. 4a because the unpaired electrons in manganese cation decreases spin–lattice relaxation times in Al nuclear, resulting in peak broadening in conjunction with intensity loss.

McMillan et al. [34] investigated the environment of Al in the $CaO–Al_2O_3$ binary system of different alumina content using ^{27}Al NMR spectra. They presented isotropic chemical shifts at about 75 ppm, 44 ppm and 13 ppm that correspond to $[AlO_4]$, $[AlO_5]$ and $[AlO_6]$ structural units, respectively. Neuville et al. [35] investigated the structure of aluminate in the $CaO–SiO_2–Al_2O_3$ system via application of ^{27}Al high-resolution solid-state NMR spectroscopy in conjunction with Raman spectroscopy. They propose that the isotropic chemical shifts in the range 67–71 ppm, 34–40 ppm and

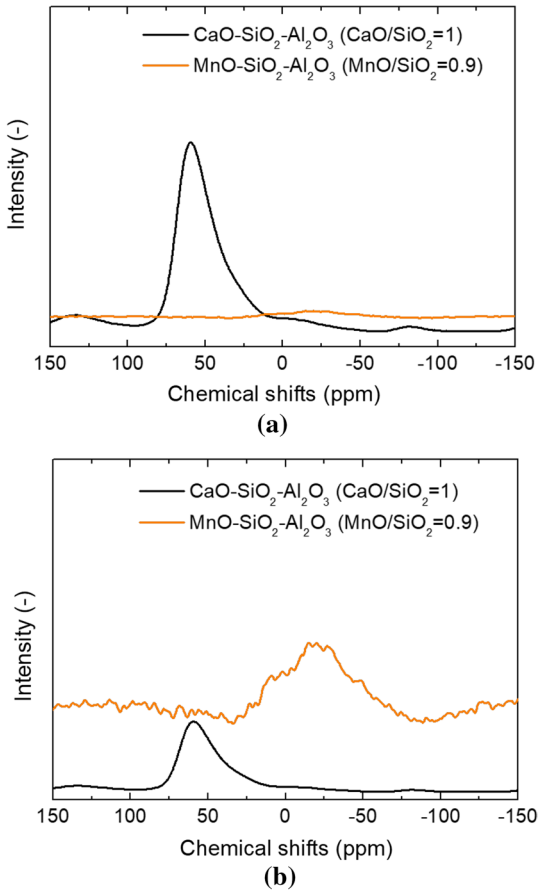

Fig. 4 **a** ^{27}Al NMR spectra and **b** normalized ^{27}Al NMR spectra of both $CaO–SiO_2–Al_2O_3$ and $MnO–SiO_2–Al_2O_3$ systems

7–11 ppm correspond to $[AlO_4]$, $[AlO_5]$ and $[AlO_6]$ structural units, respectively, and that the proportion of $[AlO_4]$ is at least 87.4% in the $CaO–SiO_2–Al_2O_3$ system ($CaO/SiO_2 = 1$, $Al_2O_3 = 3$–33 mol%). ^{27}Al NMR spectra of the $CaO–SiO_2–Al_2O_3$ system in Fig. 4a shows a maximum peak at about 60 ppm with a shoulder at about 30 ppm suggesting that the coordination number of Al atoms is 4 by majority with a small portion of $[AlO_5]$ units. This is similar to the results of Neuville et al. [35] in that the $[AlO_4]$ species are coexistent with few $[AlO_5]$ species in the $CaO–SiO_2–Al_2O_3$ system ($CaO/SiO_2 = 1$, $Al_2O_3 = 14$ mol%).

The normalized ^{27}Al NMR spectra of both $CaO–SiO_2–Al_2O_3$ and $MnO–SiO_2–Al_2O_3$ systems are shown in Fig. 4b. The chemical shifts of the $CaO–SiO_2–Al_2O_3$ have maximum peaks at around 60 ppm in ^{27}Al NMR spectra, while the chemical shifts of $MnO–SiO_2–Al_2O_3$ peak at around −25 ppm in ^{27}Al NMR spectra. For manganese containing Li-phosphate olivine crystals, the manganese cation strongly causes the paramagnetic shifts in ^{7}Li and ^{31}P NMR spectra [13, 19]. Because it was clearly revealed by the present authors in previous studies that the Mn^{2+} ion in aluminosilicate glass acts as a network modifier as does Ca^{2+} ion

[6–9], the environment of Al atoms in the aluminosilicate networks of the MnO–SiO_2–Al_2O_3 system may be similar to that in the CaO–SiO_2–Al_2O_3 system. Therefore, we can presume that isotropic chemical shifts at around 10 ppm correspond to [AlO_4], while the chemical shifts at around − 25 ppm correspond to highly coordinated aluminum, [AlO_5] or [AlO_6], in Mn–aluminosilicate glass.

3.2 Structural Changes of MnO–SiO_2–Al_2O_3 System with Different MnO/SiO_2 Ratios

The Raman bands of the MnO–SiO_2–Al_2O_3 system with different MnO/SiO_2 (= M/S) ratios are shown as a function of wavenumber in Fig. 5. The Raman bands in the 850–1200 cm^{-1} range of the M/S = 2.2 (molar ratio) system exhibit a maximum near 900 cm^{-1} with a shoulder at about 1000 cm^{-1}. The Raman bands at 900–1100 cm^{-1} increase with increasing SiO_2 content. The Raman bands at 850–1100 cm^{-1} in aluminosilicate melts and glasses are assigned to asymmetric Si–O stretching vibration; that is, Raman bands at 850–880 cm^{-1}, 900–920 cm^{-1}, 950–1000 cm^{-1}, and 1050–1100 cm^{-1} correspond to Q^0_{Si} (NBO/Si = 4), Q^1_{Si} (NBO/Si = 3), Q^2_{Si} (NBO/Si = 2), and Q^3_{Si} (NBO/Si = 1), respectively [6–9, 36–38].

Park et al. [6–9] investigated the structure–property (viscosity, capacity, density and electrical conductivity) relationships of the CaO–MnO–SiO_2 system with different SiO_2 content by analyzing the Raman spectra. They proposed that the substitution of Mn^{2+} for Ca^{2+} results in a decrease of the Q^3/Q^2 ratio, which typically presents the degree of polymerization of the silicate networks, especially in the wollastonite primary system. The Raman bands around 950–1100 cm^{-1} representing Q^2 and Q^3 in the M/S = 0.9 system become wider than those in the M/S = 2.2 system (Fig. 5), indicating that the more polymerized silicate networks, as expected, increase the contributions to the high energy side of the 950–1100 cm^{-1} envelop in the glass with higher SiO_2 and lower modifier oxide additions.

Furthermore, the Raman band at 500–600 cm^{-1} in the M/S = 0.9 system is relatively wide, while the Raman bands at about 600 cm^{-1} in the M/S = 2.2 system exhibit a single narrow peak. Several authors report that these Raman bands are corresponding to the bending motion of bridging oxygen within T–O–T (T = Si or Al) linkages [36–40]. The broadening and rising of Raman bands at 400–600 cm^{-1} with a decrease in the M/S ratio is caused by an increase in the angle of T–O–T linkages, which means the number of bridging oxygen within T–O–T become larger in M/S = 0.9 than M/S = 2.2.

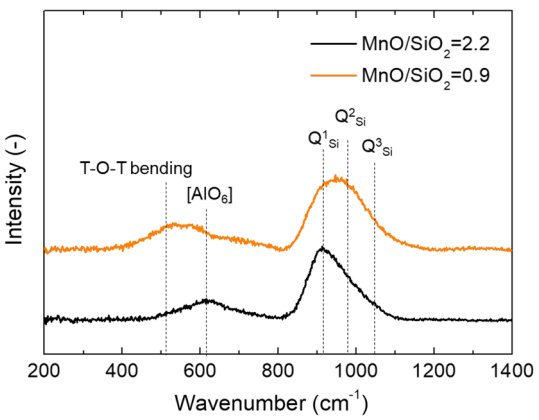

Fig. 5 Raman scattering of the MnO–SiO_2–Al_2O_3 system with different MnO/SiO_2 ratio

3.3 Effect of Ce_2O_3 on Structure of Mn–Aluminosilicate: MnO/SiO_2 = 2.2 (Molar Ratio) System

For corundum (α-Al_2O_3) and boehmite (γ-AlOOH) crystals, which are consist of that Al atoms are octahedrally coordinated, the Al–O stretching vibration of [AlO_6]-octahedron is observed in the range of 500–600 cm^{-1} Raman bands [41–43]. Tarte [42] investigated infra-red (IR) spectra of the crystal structure of aluminate compounds and proposed that the IR band at 750–900 cm^{-1} correlates with the stretching vibration of the edge sharing [AlO_4]-tetrahedral and the IR band at 650–800 cm^{-1} correlates with the stretching vibration of corned sharing [AlO_4]-tetrahedral unit. In the case of [AlO_6]-octahedron, the IR bans shifts from 500–680 cm^{-1} range to 400–530 cm^{-1} range when the edge sharing [AlO_6]-octahedron is changed to the corner sharing [AlO_6]-octahedron. Poe et al. [44, 45] observed the IR absorption bands of $CaAl_2O_4$ glass with a maximum near 820 cm^{-1} and a shoulder near 680 cm^{-1} due to the stretching vibration of the [AlO_4]-tetrahedral unit. The Raman bands at 730, 780 and 850 cm^{-1} were associated with the Al-O stretching vibration in the [AlO_4]-tetrahedral units with Q^2_{Al} (NBO/Al = 2), Q^3_{Al} (NBO/Al = 1) and Q^4_{Al} (NBO/Al = 0), respectively, in a low-SiO_2 Ca-aluminosilicate system [39, 40].

The effect of cerium addition on the Raman spectra of the MnO–SiO_2–Al_2O_3 (M/S = 2.2, Al_2O_3 = 15 mol%) system is shown in Fig. 6. In the MnO–SiO_2–Al_2O_3 ternary system, Raman bands in the 800–1100 cm^{-1} range exhibit a peak near 900 cm^{-1} and a shoulder near 1000 cm^{-1}. Because Raman bands with maximum peak near 900 cm^{-1} indicate that relative fractions of depolymerized silicate units (i.e., Q^0_{Si} [850–880 cm^{-1}] and Q^1_{Si} [900–920 cm^{-1}]) are in majority, it can be stated that the silicate networks are depolymerized in the present ternary system. Moreover, the Raman band near 600–700 cm^{-1} is assigned to the depolymerized [AlO_4]-tetrahedral unit, which indicates that the aluminate networks are also depolymerized in the Ce-free

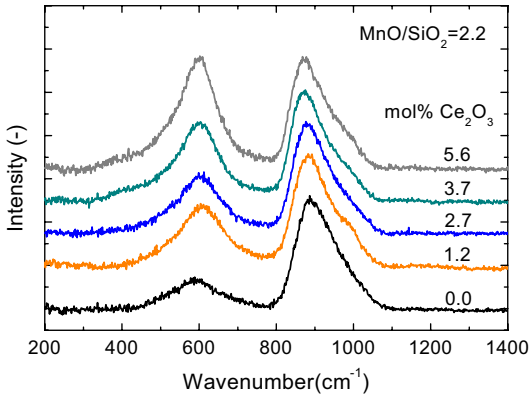

Fig. 6 Effect of Ce_2O_3 addition on the Raman scattering of the Mn–aluminosilicate system at $MnO/SiO_2 = 2.2$

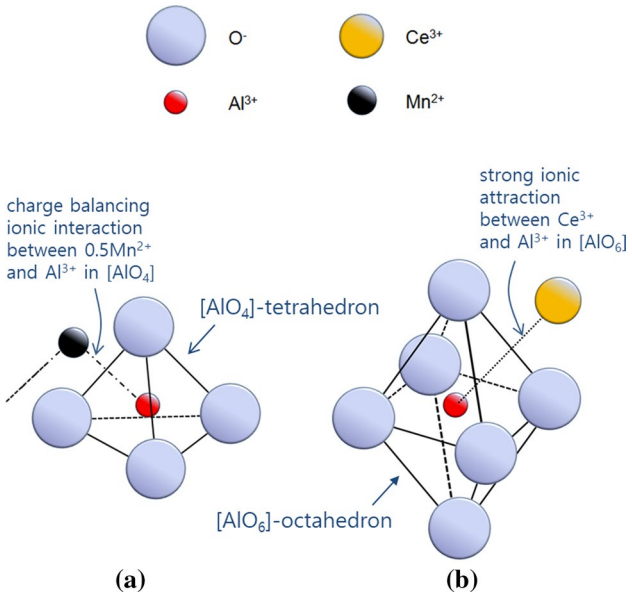

Fig. 7 Schematics of the ionic structure of **a** the $[AlO_4]$-tetrahedron balanced with $0.5Mn^{2+}$ ion (hypothetically shown as $[AlO_4]^{-}$:$0.5Mn^{2+}$ complex) and **b** the $[AlO_6]$-octahedron balanced with Ce^{3+} ion (hypothetically shown as $[AlO_6]^{3-}$:Ce^{3+} complex)

$MnO–SiO_2–Al_2O_3$ ($M/S = 2.2$, $Al_2O_3 = 15$ mol%) ternary system.

The shape of the Raman bands at 800–1100 cm^{-1}, assigned to Si–O stretching vibration with different NBOs, does not change irrespective of cerium content, indicating that cerium oxide does not affect the silicate networks in Mn–aluminosilicates. On the other hand, a sharp increase in Raman band intensity at around 600 cm^{-1} corresponding to the $[AlO_6]$-octahedral unit indicates that Ce_2O_3 strongly interacts with the aluminate unit in the Mn–aluminosilicate system. This represents a drastic change in the structure of aluminate units irrespective of changes in alumina and silica content with increasing cerium content.

The aluminate anion mainly exists as $[AlO_4]$-tetrahedron in a high M/S(=2.2) system, in which it is balanced with a half mole of charge balancing Mn^{2+} cations (i.e., expressed as hypothetical $[AlO_4]^{-}$:$0.5Mn^{2+}$ unit similar to $[SiO_4]$-unit) as schematically shown in Fig. 7a. However, when Ce_2O_3 is added, the $[AlO_6]$-octahedron becomes more stable than the $[AlO_4]$-tetrahedral unit because Ce^{3+} ion has a preferential charge balance role to $[AlO_n]$-units, resulting in formation of the hypothetical $[AlO_6]^{3-}$:Ce^{3+} unit as shown in Fig. 7b. The interaction between ionic species is presumably expressed by the following Eq. (1).

$$[AlO_4]^{-}:0.5Mn^{2+} + Ce^{3+} + 2O^{2-} = [AlO_6]^{3-}:Ce^{3+} + 0.5Mn^{2+} \quad (1)$$

Tarte [42] presented IR bands at 400–680 cm^{-1} as corresponding to the stretching vibration of $[AlO_6]$-octahedron species in the aluminate crystal. Moreover, Okuno et al. [38] recently observed the band at 600–700 cm^{-1} in aluminosilicate melts and glasses, which is due to the symmetric stretching vibrations of $[AlO_6]$-octahedron species. Therefore, the significant increase in the relative intensity of Raman bands at about 600 cm^{-1}, as shown in Fig. 6, with increasing cerium content can be attributed to the strong affinity between Al_2O_3 and Ce_2O_3, as shown in Eq. (1).

^{27}Al NMR spectra of the $MnO–SiO_2–Al_2O_3–Ce_2O_3$ system are shown in Fig. 8 with varying Ce_2O_3 content from 0 to 5.6 mol%. The peak of ^{27}Al NMR spectra moves from around 0 to −25 ppm as Ce_2O_3 is added to the $MnO–SiO_2–Al_2O_3$. For Ce-doped YAG crystals, paramagnetically shifted peaks for $[AlO_6]$ were observed at around −15 and −30 ppm in ^{27}Al MAS NMR spectra resulting from neighbored Ce^{3+} cation near aluminum nuclei [18, 22, 24]. The introduction of Ce^{3+} cation to the $MnO–SiO_2–Al_2O_3$ system modifies the $[AlO_4]$-tetrahedron balanced by Mn^{2+}

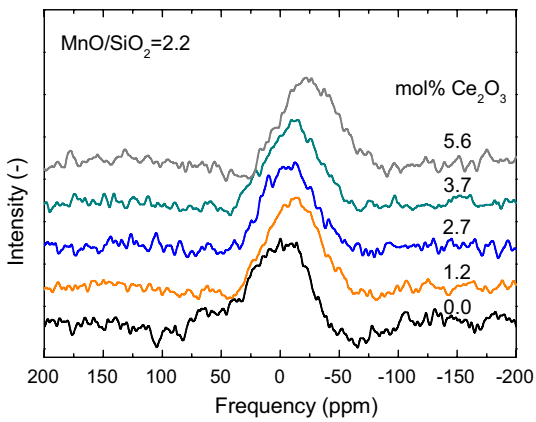

Fig. 8 Effect of Ce_2O_3 addition on ^{27}Al NMR spectra of the Mn–aluminosilicate system at $MnO/SiO_2 = 2.2$

cation into the $[AlO_6]$-octahedron balanced by Ce^{3+} cation as shown in Eq. (1). Therefore, an increase in the shifts of ^{27}Al NMR spectra from −10 to −25 ppm with addition of Ce_2O_3 indicates the formation of the $[AlO_6]^{3-}$:Ce^{3+} octahedron in the present $MnO–SiO_2–Al_2O_3–Ce_2O_3$ (M/S = 2.2) system.

The percentage of oxygen species, viz. free oxygen (O^{2-}), non-bridging oxygen (O^-), and bridging oxygen (O^0), obtained by XPS analysis for the $MnO–SiO_2–Al_2O_3–Ce_2O_3$ (M/S = 2.2) system is plotted against cerium oxide content in Fig. 9. Non-bridging oxygen represents the majority due to the availability of network-modifying Mn^{2+} cations, and this majority increases with increasing content of cerium oxide, and vice versa for free oxygen. The percentage of bridging oxygen is independent of cerium oxide content. Consequently, in the high M/S(= 2.2) system, the pre-existing $[AlO_4]^-$:$0.5Mn^{2+}$ units (Fig. 7a) could be converted to $[AlO_6]^{3-}$:Ce^{3+} units (Fig. 7b) by employing free oxygen as the content of Ce^{3+} ions increase as given in Eq. (1).

3.4 Effect of Ce_2O_3 on Structure of Mn–Aluminosilicate: $MnO/SiO_2 = 0.9$ (Molar Ratio) System

The effect of cerium addition on the Raman spectra of the high-silica Mn–aluminosilicate system (i.e., M/S = 0.9, Al_2O_3 = 14 mol%) is shown in Fig. 10. When Ce_2O_3 is added to the M/S = 0.9 system, no critical changes are observed in Raman spectra in the 800–1200 cm^{-1} range corresponding to Si–O stretching vibration because Ce^{3+} cations rarely affect silicate networks, as mentioned previously. Raman spectra at 600–800 cm^{-1}, assigned to Al–O stretching vibration, is not also significantly changed by cerium addition, which is contrary to the experimental results in the low-silica Mn–aluminosilicate system (M/S = 2.2, Al_2O_3 = 15 mol%) as discussed in Sect. 3.3. As discussed in Sect. 3.1, the existence of highly

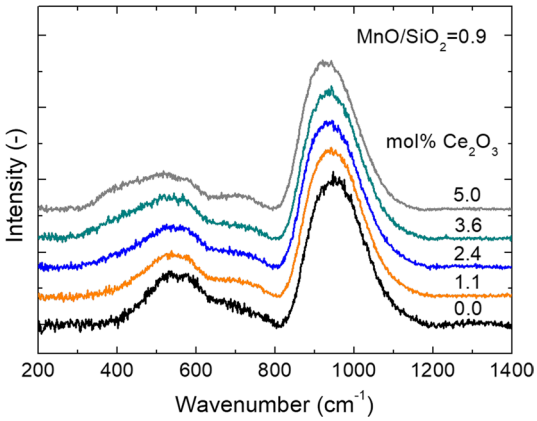

Fig. 10 Effect of Ce_2O_3 addition on the Raman scattering of the Mn–aluminosilicate system at $MnO/SiO_2 = 0.9$

coordinated aluminum other than the $[AlO_4]$-unit was noted in the M/S = 0.9 system from the analysis of ^{27}Al NMR spectra. Because Ce^{3+} cation balances $[AlO_6]$-octahedron is more advantage than $[AlO_4]$-tetrahedron in view of charge balancing, the Ce^{3+} cation preferentially reacts with pre-existing $[AlO_6]$-units in the high-silica Mn–aluminosilicate system. Therefore, the addition of Ce_2O_3 to M/S = 0.9 system results in minimal changes to Raman bands assigned to $[AlO_6]$-octahedron units (Fig. 10).

The ^{27}Al NMR spectra of the $MnO–SiO_2–Al_2O_3–Ce_2O_3$ system are shown in Fig. 11 by Ce_2O_3 concentration. The ^{27}Al NMR peak for the $MnO–SiO_2–Al_2O_3$ ternary system without Ce_2O_3 is located near −25 ppm, which indicates that $[AlO_6]$-octahedron units are mainly distributed in the high-silica Mn–aluminosilicate system. Because $[AlO_6]$-octahedron already exists in the Ce-free ternary system, Ce^{3+} does not need to convert $[AlO_4]^-$:$0.5Mn^{2+}$ tetrahedron units to $[AlO_6]^{3-}$:Ce^{3+} octahedron units in the M/S = 0.9 system. Consequently, the structure of the

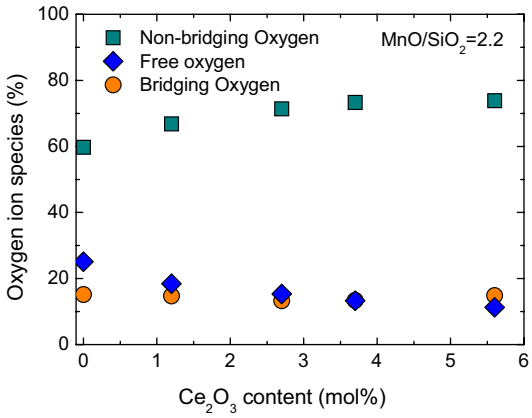

Fig. 9 Effect of Ce_2O_3 addition on the percentage of oxygen species from O1s XPS in the Mn–aluminosilicate system at $MnO/SiO_2 = 2.2$

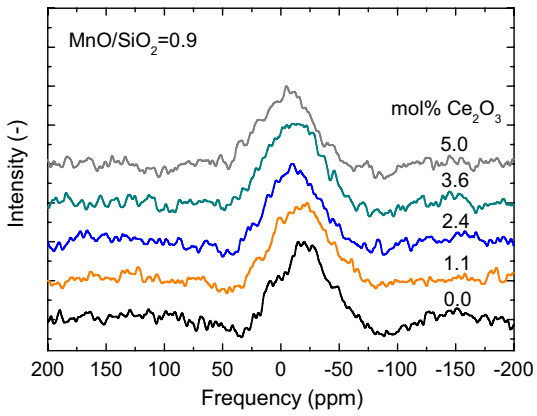

Fig. 11 Effect of Ce_2O_3 addition on ^{27}Al NMR spectra of the Mn–aluminosilicate system at $MnO/SiO_2 = 0.9$

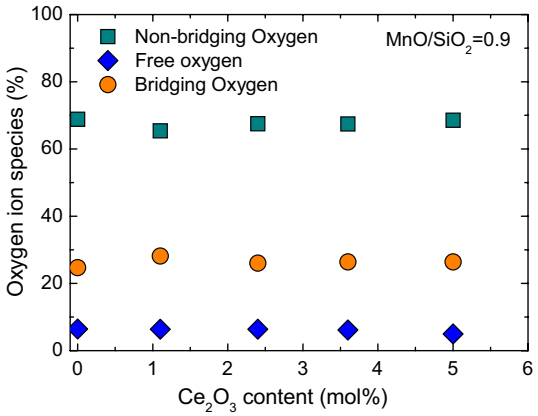

Fig. 12 Effect of Ce_2O_3 addition on the percentage of oxygen species from O1s XPS in the Mn–aluminosilicate system at $MnO/SiO_2 = 0.9$

$MnO–SiO_2–Al_2O_3–Ce_2O_3$ (M/S = 0.9, Al_2O_3 = 14 mol%) system is minimally changed by cerium addition as experimentally confirmed by Raman and ^{27}Al NMR spectra.

The deconvolution results of the O1s peak in the $MnO–SiO_2–Al_2O_3–Ce_2O_3$ (M/S = 0.9) system are shown in Fig. 12 as a function of Ce_2O_3 content. The percentage of free oxygen (O^{2-}) in this system is significantly lower than that of the M/S = 2.2 system (Fig. 9), whereas the percentage of bridging oxygen (O^0) is much higher than that of the M/S = 2.2 system (Fig. 9) because the aluminosilicate networks are more polymerized in high-silica Mn–aluminosilicate system. The relative percentages of the three oxygen species present are nearly constant irrespective of Ce_2O_3 content, which indicates that Ce_2O_3 has minimal effects on aluminosilicate networks in the high-silica system.

The Al–O bond mainly has an octahedral coordination under the condition of deficiency of charge balancing cations, i.e., in high-silica glass [34, 35, 45–48]. Before adding Ce_2O_3, the concentration of $[AlO_6]$-units in the M/S = 0.9 system are relatively greater than in the M/S = 2.2 system. Thus, Ce^{3+} ions added to high-silica Mn–aluminosilicate system instantly interact with large amounts of $[AlO_6]$-octahedron units to form more stable $[AlO_6]^{3-}$:Ce^{3+} units due to strong affinity between Ce^{3+} and Al^{3+} in $[AlO_6]$-units (Fig. 7b). Therefore, the structure of the high-silica Mn–aluminosilicate system was not significantly disturbed by the addition of Ce_2O_3.

4 Conclusions

The structure of the $MnO–SiO_2–Al_2O_3–Ce_2O_3$ systems with different MnO/SiO_2 (=M/S) ratios has been analyzed using micro-Raman spectroscopy, ^{27}Al NMR spectroscopy and XPS spectroscopy. In the present study, high-resolution solid-state NMR spectroscopy was used to elucidate the effect of Ce_2O_3 on aluminate configuration in a Mn–aluminosilicate system. The polymerization of silicate networks in the $MnO–SiO_2–Al_2O_3–Ce_2O_3$ system is strongly dependent on the M/S ratio. Because Ce^{3+} ion has a strong affinity with aluminate in aluminosilicate melts, the $[AlO_4]^-$:$0.5Mn^{2+}$ units are transformed to $[AlO_6]^{3-}$:Ce^{3+} units by employing free oxygen when Ce_2O_3 is added to the low-silica Mn–aluminosilicate system (M/S = 2.2). Thus, significant changes in aluminate structure occur upon the addition of Ce_2O_3 in the M/S = 2.2 system. However, the aluminosilicate networks of high-silica Mn–aluminosilicate systems (M/S = 0.9) are highly polymerized in conjunction with the existence of $[AlO_6]$-octahedron units due to lack of a charge compensator, i.e., Mn^{2+}. The Ce^{3+} ion has strong interactions with pre-existing $[AlO_6]$-octahedron units when Ce_2O_3 is added to this system. Therefore, structural changes were not observed despite the addition of Ce_2O_3 to Mn–aluminosilicate (M/S = 0.9) system.

Acknowledgements This research was supported by the Basic Science Research Program through the National Research Foundation of Korea (NRF) funded by the Ministry of Education (Grant Number NRF-2012R1A1A2041774). The authors thank Prof. Sung-Keun Lee, School of Earth and Environmental Sciences, Seoul National University, Korea, as well as Prof. Jonathan F. Stebbins, Department of Geological Sciences, Stanford University, USA, for the discussion of the paramagnetic phenomena and ^{27}Al NMR spectra in the present study.

References

1. S.T. Kim, S.H. Jeon, I.S. Lee, Y.S. Park, Effects of rare earth metals addition on the resistance to pitting corrosion of super duplex stainless steel—part 1. Corros. Sci. **52**, 1897–1904 (2010)
2. J. Lu, G. Cheng, Y. Che, L. Wang, G. Xiong, Effect of oxides on characteristics of MnS and transverse mechanical properties in commercial Al-killed non-quenched and tempered steel. Met. Mater. Int. **25**, 473–486 (2019)
3. N.M. Anacleto, H.G. Lee, P.C. Hayes, Sulphur Partition between $CaO–SiO_2–Ce_2O_3$ Slags and Carbon-saturated Iron. ISIJ Int. **33**, 549–555 (1993)
4. X. Yang, H. Long, G. Cheng, C. Wu, B. Wu, Effect of refining slag containing Ce_2O_3 on steel cleanliness. J. Rare Earths **29**, 1079–1083 (2011)
5. S.J. Jeong, T.S. Kim, J.H. Park, Relationship Between Sulfide Capacity and Structure of $MnO–SiO_2–Al_2O_3–Ce_2O_3$ System. Metall. Mater. Trans. B **48**, 545–553 (2016)
6. J.H. Park, Sulfide capacity and excess free energy of $CaO–SiO_2–MnO$ slag derived from structural analysis of Raman spectra. ISIJ Int. **52**, 2303–2304 (2012)
7. J.H. Park, Composition–structure–property relationships of CaO–MO–SiO_2 (M = Mg^{2+}, Mn^{2+}) systems derived from micro-Raman spectroscopy. J. Non-Cryst. Solids **358**, 3096–3102 (2012)
8. J.H. Park, Effect of silicate structure on thermodynamic properties of calcium silicate melts: quantitative analysis of Raman spectra. Met. Mater. Int. **19**, 577–584 (2013)
9. J.H. Park, Competitive dissolution mechanism of sulfur in Ca–Mn–silicate melts: structural view. Steel Res. Int. **84**, 664–669 (2013)

10. C.P. Grey, C.M. Dobson, A.K. Cheetham, R.J.B. Jakeman, Studies of rare-earth stannates by ^{119}Sn MAS NMR: the use of paramagnetic shift probes in the solid state. J. Am. Chem. Soc. **111**, 505–511 (1989)
11. C.P. Grey, M.E. Smith, A.K. Cheetham, C.M. Dobson, R. Dupree, ^{89}Y MAS NMR study of rare-earth pyrochlores: paramagnetic shifts in the solid state. J. Am. Chem. Soc. **112**, 4670–4675 (1990)
12. I. Bertini, C. Luchinat, G. Parigi, Magnetic susceptibility in paramagnetic NMR. Prog. Nucl. Magn. Reson. Spectrosc. **40**, 249–273 (2002)
13. S.L. Wilcke, Y.J. Lee, E.J. Cairns, J.A.J.A.M.R. Reimer, Covalency measurements via NMR in lithium metal phosphates. Appl. Magn. Reson. **32**, 547–563 (2007)
14. J.F. Stebbins, K.E. Kelsey, Anomalous resonances in ^{29}Si and ^{27}Al NMR spectra of pyrope ($[Mg, Fe]_3Al_2Si_3O_{12}$) garnets: effects of paramagnetic cations. Phys. Chem. Chem. Phys. **11**, 6906–6917 (2009)
15. H.I. Kim, S.K. Lee, The effect of iron content on the atomic structure of alkali silicate glasses using solid-state NMR spectroscopy. J. Miner. Soc. Korea **24**, 301–312 (2011)
16. A.C. Palke, J.F. Stebbins, Variable-temperature ^{27}Al and ^{29}Si NMR studies of synthetic forsterite and Fe-bearing Dora Maira pyrope garnet: temperature dependence and mechanisms of paramagnetically shifted peaks. Am. Miner. **96**, 1090–1099 (2011)
17. A.C. Palke, J.F. Stebbins, Paramagnetic interactions in the ^{31}P NMR spectroscopy of rare earth element orthophosphate ($REPO_4$, monazite/xenotime) solid solutions. Am. Miner. **96**, 1343–1353 (2011)
18. N.C. George, A.J. Pell, G. Dantelle, K. Page, A. Llobet, M. Balasubramanian, G. Pintacuda, B.F. Chmelka, R. Seshadri, Local environments of dilute activator ions in the solid-state lighting phosphor $Y_{3-x}Ce_xAl_5O_{12}$. Chem. Mater. **25**, 3979–3995 (2013)
19. D.S. Middlemiss, A.J. Ilott, R.J. Clément, F.C. Strobridge, C.P. Grey, Density functional theory-based bond pathway decompositions of hyperfine shifts: equipping solid-state NMR to characterize atomic environments in paramagnetic materials. Chem. Mater. **25**, 1723–1734 (2013)
20. R.J. McCarty, A.C. Palke, J.F. Stebbins, J.S. Hartman, Transition metal cation site preferences in forsterite (Mg_2SiO_4) determined from paramagnetically shifted NMR resonances. Am. Miner. **100**, 1265–1276 (2015)
21. H.I. Kim, J.C. Sur, S.K. Lee, Effect of iron content on the structure and disorder of iron-bearing sodium silicate glasses: a high-resolution ^{29}Si and ^{17}O solid-state NMR study. Geochim. Cosmochim. Acta **173**, 160–180 (2016)
22. R.J. McCarty, J.F. Stebbins, Investigating lanthanide dopant distributions in yttrium aluminum garnet (YAG) using solid state paramagnetic NMR. Solid State Nucl. Magn. Reson. **79**, 11–22 (2016)
23. J.F. Stebbins, Toward the wider application of 29Si NMR spectroscopy to paramagnetic transition metal silicate minerals: copper(II) silicates. Am. Miner. **102**, 2406–2414 (2017)
24. J.F. Stebbins, R.J. McCarty, A.C. Palke, Solid-state NMR and short-range order in crystalline oxides and silicates: a new tool in paramagnetic resonances. Acta Crystallogr. C Struct. Chem. **73**, 128–136 (2017)
25. J.F. Stebbins, R.J. McCarty, A.C. Palke, Toward the wider application of ^{29}Si NMR spectroscopy to paramagnetic transition metal silicate minerals and glasses: Fe(II), Co(II), and Ni(II) silicates. Am. Miner. **103**, 776–791 (2018)
26. S.L. Lin, C.S. Hwang, Structures of CeO_2–Al_2O_3–SiO_2 glasses. J. Non-Cryst. Solids **202**, 61–67 (1996)
27. S.L. Lin, C.S. Hwang, J.F. Lee, Structure and properties of CeO_2–Al_2O_3–SiO_2 Glasses. Jpn. J. Appl. Phys. **35**, 3975–3983 (1996)
28. P. Wu, A.D. Pelton, Coupled thermodynamic-phase diagram assessment of the rare earth oxide-aluminium oxide binary systems. J. Alloys Compd. **179**, 259–287 (1992)
29. S. Ueda, K. Morita, N. Sano, Activity of $AlO_{1.5}$ for the CaO–$AlO_{1.5}$–$CeO_{1.5}$ system at 1 773 K. ISIJ Int. **38**, 1292–1296 (1998)
30. R. Kitano, M. Ishii, M. Uo, K. Morita, Thermodynamic properties of the CaO–$AlO_{1.5}$–$CeO_{1.5}$ system. ISIJ Int. **56**, 1893–1901 (2016)
31. Y. Kaneko, Y. Suginohara, Fundamental studies on quantitative analysis of O^0, O^- and O^{2-} ions in silicate by X-ray photoelectron spectroscopy. J. Jpn. Inst. Met. **41**, 375–380 (1977)
32. J.H. Park, P.C.-H. Rhee, Ionic properties of oxygen in slag. J. Non-Cryst. Solids **282**, 7–14 (2001)
33. S.H. Chung, I. Sohn, *Effect of NaF and CaO/SiO$_2$ mass pct. on the hydrogen dissolution behavior in calcium-silicate-based molten fluxes* (Met. Mater. Int. 2019). https://doi.org/10.1007/s12540-019-00296-1
34. P.F. McMillan, W.T. Petuskey, B. Coté, D. Massiot, C. Landron, J.P. Coutures, A structural investigation of CaO–Al_2O_3 glasses via ^{27}Al MAS-NMR. J. Non-Cryst. Solids **195**, 261–271 (1996)
35. D.R. Neuville, L. Cormier, D. Massiot, Al coordination and speciation in calcium aluminosilicate glasses: effects of composition determined by ^{27}Al MQ-MAS NMR and Raman spectroscopy. Chem. Geol. **229**, 173–185 (2006)
36. P. McMillan, B. Piriou, A. Navrotsky, A Raman spectroscopic study of glasses along the joins silica-calcium aluminate, silica-sodium aluminate, and silica-potassium aluminate. Geochim. Cosmochim. Acta **46**, 2021–2037 (1982)
37. F.A. Seifert, B.O. Mysen, D. Virgo, Three-dimensional network structure of quenched melts (glass) in the systems SiO_2–$NaAlO_2$, SiO_2–$CaAl_2O_4$ and SiO_2–$MgAl_2O_4$. Am. Miner. **67**, 696–717 (1982)
38. M. Okuno, N. Zotov, M. Schmücker, H. Schneider, Structure of SiO_2–Al_2O_3 glasses: combined X-ray diffraction, IR and Raman studies. J. Non-Cryst. Solids **351**, 1032–1038 (2005)
39. P. McMillan, B. Piriou, Raman spectroscopy of calcium aluminate glasses and crystals. J. Non-Cryst. Solids **55**, 221–242 (1983)
40. T.S. Kim, J.H. Park, Structure-viscosity relationship of low-silica calcium aluminosilicate melts. ISIJ Int. **54**, 2031–2038 (2014)
41. S.P.S. Porto, R.S. Krishnan, Raman effect of corundum. J. Chem. Phys. **47**, 1009–1012 (1967)
42. P. Tarte, Infra-red spectra of inorganic aluminates and characteristic vibrational frequencies of AlO_4 tetrahedra and AlO_6 octahedra. Spectrochim. Acta Part A: Mol. Spectrosc. **23**, 2127–2143 (1967)
43. A.B. Kiss, G. Keresztury, L. Farkas, Raman and IR spectra and structure of boehmite (γ-AlOOH). Evidence for the recently discarded D_{2h}^{17} space group. Spectrochim. Acta Part A: Mol. Spectrosc. **36**, 653–658 (1980)
44. B.T. Poe, P.F. McMillan, C.A. Angell, R.K. Sato, Al and Si coordination in SiO_2-Al_2O_3 glasses and liquids: a study by NMR and IR spectroscopy and MD simulations. Chem. Geol. **96**, 333–349 (1992)
45. B.T. Poe, P.F. McMillan, B. Coté, D. Massiot, J.-P. Coutures, Structure and dynamics in calcium aluminate liquids: high-temperature ^{27}Al NMR and Raman spectroscopy. J. Am. Ceram. Soc. **77**, 1832–1838 (1994)
46. J.H. Park, D.J. Min, H.S. Song, Amphoteric behavior of alumina in viscous flow and structure of CaO–SiO_2(–MgO)–Al_2O_3 slags. Metall. Mater. Trans. B **35**, 269–275 (2004)
47. D.J. Min, F. Tsukihashi, Recent advances in understanding physical properties of metallurgical slags. Met. Mater. Int. **23**, 1–19 (2017)
48. J.S. Han, Y. Chung, J.H. Park, Influence of exposure temperature on degradation of magnesia refractory by steel refining slags. Met. Mater. Int. **25**, 1360–1365 (2019)